Facile Polyolefin Plastics Hydrogenolysis Catalyzed by a Surface Electrophilic d^0 Hydride

Authors: Alexander H. Mason,[1] Alessandro Motta,[2] Anusheela Das,[1] Qing Ma,[1] Michael J. Bedzyk,*[1] Yosi Kratish,*[1] Tobin J. Marks*[1]

Affiliations:

[1] Northwestern University, Evanston IL 60208, United States

[2] Università di Roma "La Sapienza" and INSTM, UdR Roma, Piazzale Aldo Moro 5, I-00185 Roma, Italy

*Corresponding author emails: bedzyk@northwestern.edu, yosi.kratish@northwestern.edu, t-marks@northwestern.edu

Abstract: Polyolefins comprise a major fraction of single-use plastics and yet their catalytic deconstruction/recycling has proven challenging due to their inert hydrocarbon connectivities. Here an electrophilic earth-abundant single-site organozirconium catalyst chemisorbed on a highly Brønsted acidic support and characterized by a broad array of experimental and theoretical techniques, is shown to mediate the rapid hydrogenolytic cleavage of molecular and macromolecular saturated hydrocarbons under mild conditions. For *n*-hexadecane, hydrogenolysis to light hydrocarbons proceeds with an activity of 690 mol *n*-hexadecane · mol Zr^{-1} · h^{-1} at 150°C/2.5 atm H_2 pressure. Under similar solventless conditions, polyethylene, polyethylene-*co*-1-octene, isotactic polypropylene, and a post-consumer sandwich bag are rapidly hydrogenolyzed to low molecular mass hydrocarbons *via* a turnover-limiting C-C scission pathway involving *ß*-alkyl transfer rather than more common σ-bond metathesis.

One-Sentence Summary: "An earth-abundant organo-zirconium catalyst hydrogenolyzes diverse polyolefins with high efficiency *via* well-defined pathways."

Introduction. Synthetic polymers play an important role in modern society, providing critical materials for food packaging, infrastructure and transportation, clothing, medical disposables, consumer electronics, etc. In 2018, ~395 million tons were produced, with 1.1 billion tons (Gt) projected annually by 2050 (*1, 2*). Since most plastics are single-use, global production has created a corresponding increase in derived waste and environmental impact (*3, 4*), with a cumulative 5.7 Gt of waste landfilled or incinerated to date (*2*). Recycling is an attractive but underutilized means of repurposing plastics, decreasing fossil fuels reliance, and addresing plastics pollution (*5-7*). However, today most recycling is mechanical, with polymers shredded then re-shaped into materials having inferior properties vs virgin materials (*8*). Among modern synthetic polymers, polyolefins comprise more than half of the production due to low cost, enormous versatility, and chemical inertness. Today polyolefins such as polyethylene, polypropylene, and polystyrene are typically recycled pyrolytically at temperatures > 400°C. However, this energy-intensive unselective "cracking" yields hydrocarbon mixtures and significant residual "coke" (*9*).

Catalytic polyolefin deconstruction to lighter hydrocarbons has proven challenging due to their chemical/thermal inertness. One homogeneous approach uses an Ir catalyst and metathesis with an alkane to lower the polyolefin molecular mass (*10*). Polyolefins have also been hydrogenolytically upcycled over heterogeneous precious-metal Pd, Pt, Ru or Re catalysts to wax-range and lighter hydrocarbons. Such processes typically employ high temperatures/pressures with high catalyst loadings and long reaction times (*11-17*).

Regarding earth-abundant metal polyolefin hydrogenolysis catalysts, the only example to our knowledge employed a neutral d^0 Zr alkyl bound to silica-alumina, which mediates relatively slow hydrogenolysis (**Fig. 1A**) (*18*). We envisioned that protonolytic chemisorption of Zr alkyls on highly Brønsted acidic surfaces (having weak/weakly coordinating conjugate Brønsted bases) might yield d^0 catalysts sufficiently electrophilic to efficiently cleave polyolefin C-C bonds. Note that chemisorbing $Cp^*Zr(CH_3)_3$ ($Cp^* = \eta^5$-Me_5C_5) on Brønsted acidic sulfated metal oxides yields methane + electrostatically-bound cationic adsorbates (**Fig. 1B**) which catalyze rapid arene hydrogenation and olefin polymerization (*19-21*). Such catalysts operate *via* mechanisms differing substantially from later transition metals, raising the intriguing question of whether they might rapidly activate/hydrogenolyze polyolefins through unconventional pathways.

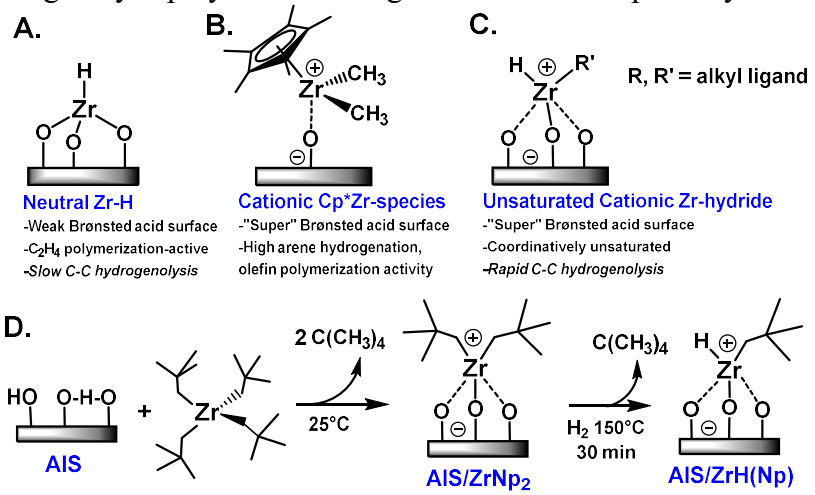

Fig. 1. Zirconium alkyl chemistry on oxide surfaces. (**A**) Zr hydrocarbyl-derived adsorbate on a weak Brønsted acid surface, (**B**) $Cp^*Zr(CH_3)_3$-derived adsorbate on a "super" Brønsted acidic surface functioning as a weak conjugate base, (**C**) Analogous $Zr(neopentyl)_4$-derived adsorbate after H_2 exposure, (**D**) $Zr(neopentyl)_4$ chemisorption on very Brønsted acidic sulfated alumina (**AlS**), and hydride generation *via* Zr-neopentyl hydrogenolysis.

Here we report that $Zr(neopentyl)_4$ chemisorption on sulfated alumina (Hammett acidity, H_0 = -14.6) (*22*) yields **AlS/ZrNp$_2$** (**Fig. 1D**), characterized by solid-state Nuclear Magnetic Resonance (NMR) and Diffuse Reflectance Infrared Fourier Transform Spectroscopy (DRIFTS), Inductively Coupled Plasma Atomic Emission Spectroscopy (ICP-AES), (X-ray Absorption Near Edge Structure (XANES), Extended X-ray Absorption Fine Structure (EXAFS), and Density-Functional Theory (DFT) computation. **AlS/ZrNp$_2$** catalyzes the rapid, solventless hydrogenolysis of polyethylene (**PE**), isotactic polypropylene (**i-PP**), polyethylene-*co*-1-octene (**PECO**) copolymer, and consumer **PE** under very mild conditions. Using hexadecane (**C16**) as a **PE** model, the mechanism is first probed before proceeding to polyolefins, and **C16** hydrogenolysis activities of 690 mol **C16**·mol Zr^{-1}·h^{-1} are achieved at 150°C/2.5 atm H_2. Rate-limiting C-C bond scission *via* ß-alkyl transfer rather than σ-bond metathesis (common in d^0 metal catalysis) (*23, 24*) predominates, in accord with DFT computation.

Catalyst Synthesis and Characterization (Details in Supplementary Materials).

AlS/ZrNp$_2$ with a Zr loading of 1.40 wt% (~0.5 Zr/nm^2) was prepared by rigorously anaerobic $Zr(neopentyl)_4$ chemisorption on **AlS**. Solid-state ^{1}H magic angle spinning (MAS) NMR spectroscopy reveals a δ 0.90 ppm signal assignable to Zr-Np CH_3 and CH_2 moieties (**Fig. 2A**). Upon H_2 exposure at 150°C/30 min, one or more neopentyl ligands are hydrogenolyzed, yielding the Zr-hydride, **AlS/ZrH(Np)** (**Figs. 1D, 2A**) with a characteristic δ11 ppm ^{1}H Zr-H NMR signal

(*25-27*), not present in D_2 reactions (**Fig. S4**). Besides weakened C-H alkyl signals, resonances at δ2.0 and δ7.5 ppm are also visible and tentatively assigned to Al-OH and Al-H groups, respectively (*28, 29*). DRIFTS spectra reveal υZr-H and υAl-H stretching modes at 1620 cm^{-1} and 1930 cm^{-1}, respectively (**Fig. 2B**) (*18, 25*) not present in **AlS** nor **AlS/ZrNp$_2$** (**Fig. 2B**). Furthermore, exposing **AlS/ZrNp$_2$** to D_2 significantly weakens these features, supporting the υZr-H and υAl-H assignments (**Fig. S5**). Additionally, the **AlS/ZrNp$_2$** 3000-2800 cm^{-1} alkyl υC-H modes weaken upon H_2 exposure, supporting Zr-neopentyl → **AlS/ZrH(Np)** conversion (**Fig. 2B**). On exposing **AlS/ZrH(Np)** to pentane vapor, the Zr-H δ11 ppm NMR signal and the 1620 cm^{-1} vibration vanish, however the signals at δ7.5 ppm and 1930 cm^{-1} remain (**Fig. S6**), arguing the latter represent less reactive Al-H species.

Zr EXAFS and DFT computation provide additional chemical and electronic structural information. The former indicates that **AlS/ZrNp$_2$** is an oxide-bound $ZrNp_2$ species having three rather long Zr-O bonds (~2.26 Å average) and two Zr-C bonds (**Figs. 2C, 2D**; **Table 1**, entry 1) DFT-derived model for **AlS/ZrNp$_2$** (**Fig. 2C**), reveals three 2.18-2.24 Å Zr-O bonds, in excellent agreement with the EXAFS (**Table 1**, entry 1). *Operando* EXAFS monitoring of **AlS/ZrNp$_2$** hydrogenolysis reveals gradual conversion to **AlS/ZrH(Np)** with the Zr-C bond number falling from 2.0 (**AlS/ZrNp$_2$**) to 1.0 (**AlS/ZrH(Np)**) and a slight Zr-O average bond length contraction to ~2.19 Å (**Figs. 2C, 2D**; **Table 1**, entry 2), consistent with the less encumbered hydride ligand replacing Np. Further H_2 treatment at 150° C effects minimal change, demonstrating that **AlS/ZrH(Np)** is stable under catalytic conditions (*vide infra*). From the DFT analysis, the three **AlS/ZrH(Np)** Zr-O bonds are slightly contracted to 2.10-2.20 Å, in accord with the EXAFS data. Additionally, the DFT-computed 1704 cm^{-1} **AlS/ZrH(Np)** υZr-H frequency compares favorably with the 1620 cm^{-1} DRIFTS value, further supporting the structure in **Figure 2C** (**Table 1**, entry 2). **AlS/ZrH(Np)** pentane exposure affords a **AlS/Zr(alkyl)$_2$** species having three Zr-O bonds and two Zr-C bonds (EXAFS), in agreement with the NMR and DRIFTS data (**Fig. 2D**).

Note that the **AlS/ZrNp$_2$** and **AlS/ZrH(Np)** Zr-O bonds are significantly elongated vs those in neutrally charged 2,6-$^{t}Bu_2PhOZr(benzyl)_3$ (Zr-O = 1.94 Å) (*30*) and $(L(Me)AlO)_2Zr(benzyl)_2$ (L = (2,6-$^{i}Pr_2C_6H_3NC(Me))_2CH$) (Zr-O = 1.91 Å; **Fig. 2C**, **Table 1**, entries 3, 4) (*31*), and formally neutrally charged SiO_2/Zr-H (1.95Å; **Fig. 1A, Table 1**, entry 5) (*32*), with shorter Zr-O bonds suggesting more covalent σ-bonding, and longer Zr-O bonds greater electrostatic character between the electron-deficient Zr centers and weakly basic **AlS** oxide ligands (*21, 33, 34*). Also, the XANES Zr K-edge energies for **AlS/ZrNp$_2$** (18.005 KeV), **AlS/ZrH(Np)** (18.008 KeV), and **AlS/Zr(alkyl)$_2$** (18.006 KeV) lie in the range of cationic complexes vs neutrally charged $^{t}Bu_2PhOZr(benzyl)_3$ (17.998 KeV) and $Zr(benzyl)_4$ (17.999 KeV) (**Fig. 2E**) (*20*). Finally, **AlS/ZrH(Np)** charge partition analysis computation (*35*) reveals that the Zr atom in model $(EtO)_2Zr(neopentyl)_2$ bears a +1.66 charge vs. +1.99 in **AlS/ZrH(Np)**. Calculated Zr-O distances are, $(EtO)_2Zr(neopentyl)_2$, 1.93 Å, and **AlS/ZrH(Np)**, 2.10-2.20 Å.

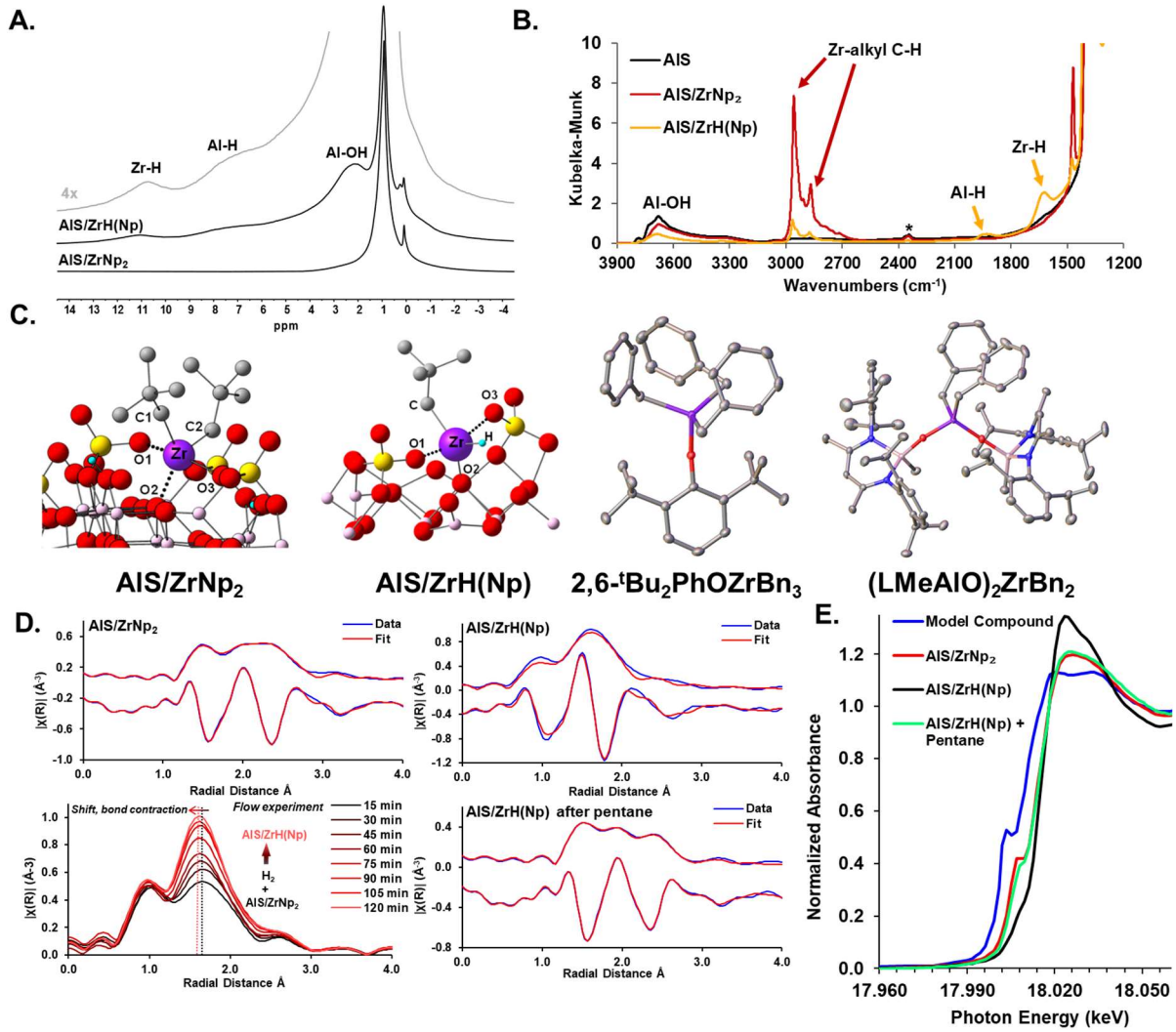

Fig. 2. Characterization of the AlS/ZrNp$_2$ adsorbate and AlS/ZrH(Np) hydrogenolysis product, and atomistic models of Zr dialkyl and alkyl hydride structures on AlS vs. neutrally charged model Zr dialkyls. (**A**) Solid-state ^{1}H MAS-NMR spectra of **AlS/ZrNp$_2$** and **AlS/ZrH(Np)**; (**B**) DRIFTS vibrational spectra of **AlS/ZrNp$_2$**, **AlS/ZrH(Np)**, and the **AlS** support. * =atmospheric CO_2 background artefact. (**C**) DFT-computed structures of **AlS/ZrNp$_2$**, **AlS/ZrH(Np),** and single-crystal diffraction structures of 4-coordinate Zr models. (**D**) EXAFS spectra of **AlS/ZrNp$_2$, AlS/ZrH(Np)**, and **AlS/ZrH(Np)** after pentane exposure (**AlS/Zr(alkyl)$_2$**), and stacked *operando* EXAFS temporal plot for **AlS/ZrNp$_2$** hydrogenolysis at 25°C. Real component of EXAFS spectra are offset by -0.3 Å^{-3}. (**E**) Zr K-edge XANES of **AlS/ZrH(Np)**, **AlS/ZrNp$_2$**, (**AlS/Zr(alkyl)$_2$**), and 2,6-^{t}Bu$_2$PhOZr(benzyl)$_3$.

Table 1. Experimental EXAFS and DRIFTS structural data for AlS/ZrNp$_2$ and AlS/ZrH(Np), and their DFT computed metrical parameters

Entry	Species	Bond	Experimental bond length (Å) [a]	DFT bond length (Å)	DRIFTS stretching freq. υ(cm^{-1})	DFT stretching freq. υ(cm^{-1})
1	AlS/ZrNp$_2$	Zr-O1	2.26(2)	2.24	Alkyl C-H	Alkyl C-H
		Zr-O2	2.26(2)	2.20	2958	3041
		Zr-O3	2.26(2)	2.18	2868	2679
		Zr-C1	2.42(3)	2.12		

		Zr-C2	2.42(3)	2.22		
2	**AlS/ZrH(Np)**	Zr-O1	2.29(3)	2.20	**Alkyl C-H**	**Alkyl C-H**
		Zr-O2	2.14(3)	2.10	2963	3040
		Zr-O3	2.14(3)	2.15	2870	2966
		Zr-C	2.38(3)	2.20	**Zr-H**	**Zr-H**
		Zr-H	N.D.	1.83	1620	1704
3	**2,6-^{t}Bu$_2$PhOZrBn$_3$**	Zr-O	1.947(1)	N.D.	N.D.	N.D.
		Zr-C [b]	2.279(2)			
4	**(LMeAlO)$_2$ZrBn$_2$**	Zr-O	1.91	N.D.	N.D.	N.D.
		Zr-O	1.91			
		Zr-C	2.26			
		Zr-C	2.28			
5[c]	**SiO$_2$/ZrH**	Zr-O [b]	1.94	N.D.	**Zr-H**	**Zr-H**
					1638	N.A.

[a] Entries 1, 2, and 3 from EXAFS; Entry 4 from single-crystal X-ray diffraction. [b] Average of 3 Zr-O bond lengths. [c] Reference (*32*).

Catalytic *n*-Hexadecane and Polyolefin Hydrogenolysis (Details in Supplementary Materials). Liquid n-hexadecane (**C16**) (b.p.= 287°C) served as a realistic **PE** reactivity/rheology model. Rapidly stirring (to minimize mass transport effects) 1.93 mL of **C16** over 178 mg of **AlS/ZrNp$_2$** (0.05 mol% Zr) at 150°C/2.5 atm H_2 (350 mL vessel) effects complete **C16** conversion to C1-C9 hydrocarbons in as little as 18 min by Gas Chromatography/Mass Spectrometry (GC/MS) and Gas Chromatography/Flame Ionization Detection (GC/FID) (**Table 2,** entries 1-4; Video S1). Note that in all **C16** hydrogenolyses, the products are linear even and odd carbon number hydrocarbons, with ~1% methyl branched alkanes (**Figs. S11-S13**). A 24h control with only **C16** + **AlS** + H_2 yielded negligible hydrogenolysis products (**Table 2**, entry 5, **Fig S8**). Kinetic studies in which **C16** conversion (at <15% conversions) was monitored as a function of H_2 pressure, catalyst loading, and time (**Fig. S9**) yielded the empirical rate law $\nu \sim k[Zr]^1[H_2]^0[\mathbf{C16}]^0$ which holds except at very low (0.005 mol%) Zr loadings where trace impurity poisoning may intrude. To our knowledge, this is the first kinetic/mechanistic study of cationic d^0 catalyst-mediated liquid alkane hydrogenolysis.

Table 2. C16 and polyolefin hydrogenolysis data over AlS/ZrH(Np).[a]

Entry	Substrate	Temperature (°C)	H_2 Pressure (atm)	Reaction time (min)	Catalyst loading (Zr mol%)	Substrate Conversion (%)	Activity (h^{-1})[b]
1	**C16**	150	2.5	18	0.05	>99	690
2	**C16**	120	4.0	15	0.02	11.5	261
3	**C16**	120	0.5	15	0.02	12	267
4	**C16**	90	2.0	90	0.02	14.9	56
5	**C16**	150	2.0	1440	0.00[c]	0	0
6	**PE**	150	2.0	30	0.06	32[d]	2088
7	**PE**	150	2.0	120	0.06	95[d]	1566
8	***i*-PP**	190	2.0	60	0.12	96[d]	2193
9	**PECO**	190	2.0	60	0.07	>99[d]	2995
10	**Sandwich bag**	190	2.0	1440	0.15	96[d]	29

[a]Reaction in 350 mL heavy-walled glass pressure vessels. Catalyst loading with respect to CH_2CH_2 units for **C16** and **PE**, C_3H_6 units for **i-PP**. [b]**C16** activity: mol(**C16**)·mol(Zr)$^{-1}$·h^{-1}; polyolefin activity: mol (CH_2CH_2 units of CH_2Cl_2-soluble hydrocarbons + volatiles)·mol(Zr)$^{-1}$·h^{-1}. [c]Control experiment without Zr. [d] Conversion = yield of combined volatiles + CH_2Cl_2-soluble hydrocarbons.

Following the **C16** experiments, linear polyethylene (**PE**) homopolymer, isotactic polypropylene (**i-PP**), polyethylene-*co*-1-octene (**PECO**), and a **PE** sandwich bag were investigated. The time dependence of **PE** hydrogenolysis with 0.06 mol% Zr was monitored at 150°C/2 atm H_2 (**Fig. 3A**), with reactions halted periodically by cooling to 25°C. Products were then extracted with CH_2Cl_2 ("DCM extract"), and the remaining partially hydrogenolyzed "solids fraction" corrected for the residual catalyst mass. A "volatile" fraction was assigned to the remaining products. While this mass could not be rigorously quantified, volatile product compositions were analyzed *via* headspace GC/FID. The results are shown in **Figs 3B** and **3C**, and in **Table 2**, entries 6 and 7. After 2 h, 96% of the hydrocarbon products are volatile or DCM-soluble and, as expected, have the shortest average chain lengths. The PE solids comprise only 4 wt% of the product as ≤60 carbon oligomers by Gel Permeation Chromatography (GPC) (**Fig. S10, Table S2**). Note the gradual decline in the most probable chain length of DCM extracts with conversion, falling from ~18 carbons (10 min) to 14 carbons (30 min), 12 carbons (50min), and 11 carbons (2h) (**Fig. 3C**). Minor alkane branching is detected and is ascribed to eliminated olefin reinsertion.

While linear **PE** homopolymer is an informative substrate due to the relatively low melting point and simple structure, **i-PP** and **PECO** are of greater technical significance (*36*). The **AlS/ZrH(Np)** catalyst was next applied to these materials at 190°C to lower the viscosity for ease of stirring. Reacting 1.0 g **i-PP** over 0.12 mol% **AlS/ZrNp$_2$** under 2 atm H_2 effects quantitative conversion to 68% low-molecular weight (M_w) (<C30) products and 28% C1-C6 volatiles in only 1h (**Table 2**, entry 8, **Figs. 3D, 3F**). The **i-PP** DCM extract chromatogram has greater complexity than **PE** since the product alkanes are not only linear and have significant ethyl- and methyl-branching, reflecting the **PP** chain cleavage point (**Fig. 3E**). The DCM extract number average molecular mass (M_n) also falls with increasing conversion and the distribution narrows as for **PE** (**Fig. 3E**). Stirring **PECO** reaction mixtures was challenged by the viscosity. Nevertheless, hydrogenolysis proceeds rapidly to yield 85% volatile and 15% DCM soluble/low-M_w alkanes within 1 h (**Fig. 3F**). The 1 h and 2 h GC/MS data are similar, probably reflecting H_2 starvation, and yielding a most probable chain length of ~15 carbons (**Fig. 3G**). Low-level alkane branching is present (~1%), probably from the enchained 1-octene comonomer. Finally, near complete hydrogenolysis (96% conversion) of commercial post-consumer sandwich bags is achieved for 190°C/2 atm H_2/0.15 mol% Zr loading in 20 h.

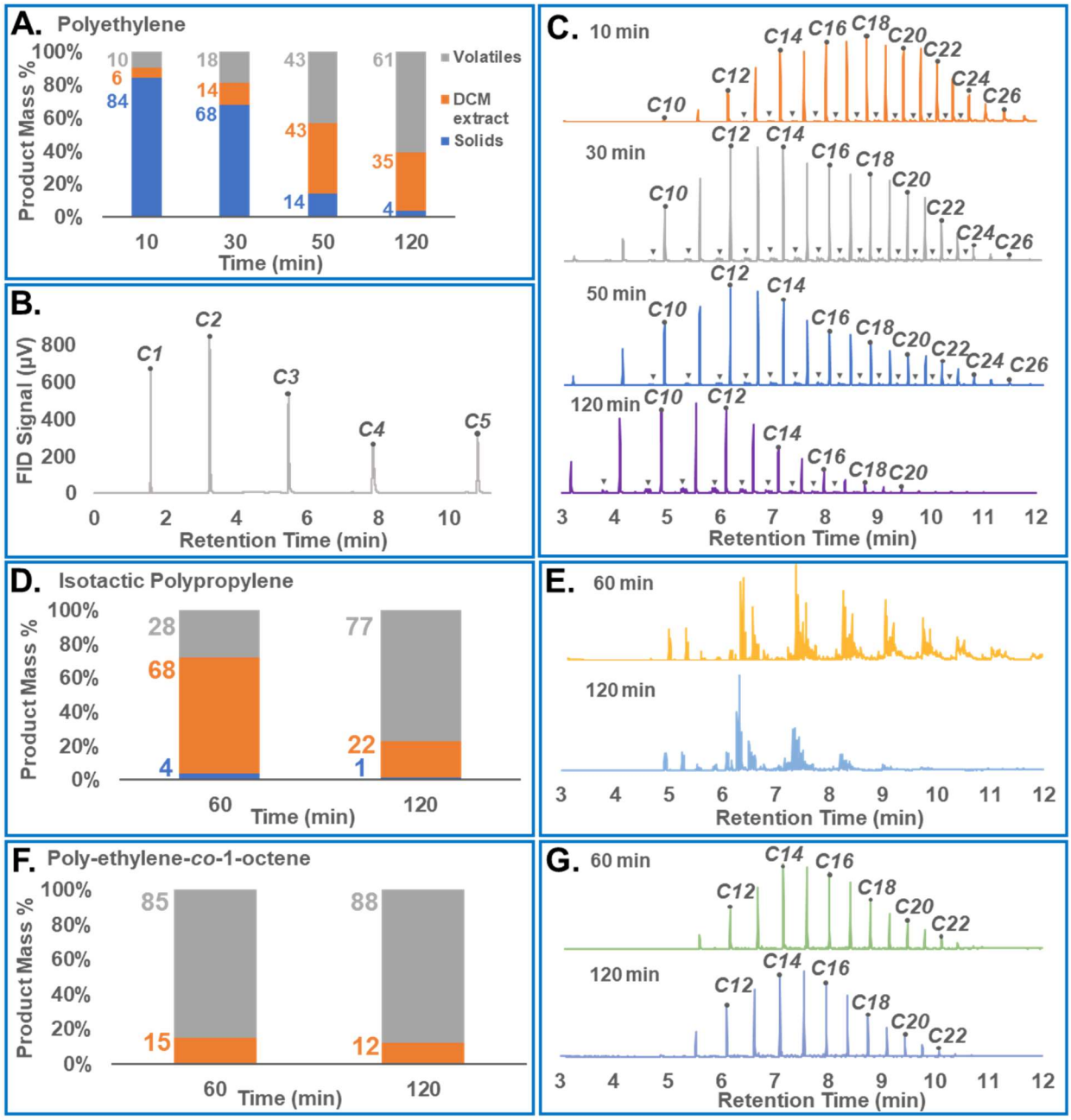

Fig. 3. Catalytic hydrogenolysis of technically relevant polyolefins. (**A**) Temporal product distributions for **AlS/ZrNp$_2$**-catalyzed hydrogenolysis of linear **PE** (150° C, 2.0 atm H_2, 0.06 mol% Zr). (**B**) Headspace GC/FID chromatogram of 30 min **PE** hydrogenolysis. (**C**) GC/MS chromatograms of DCM extracts from **AlS/ZrNp$_2$**-catalyzed **PE** hydrogenolyses. Trace chain branching denoted is by "▼". (**D**) Temporal product distributions for the **AlS/ZrNp$_2$**-catalyzed **i-PP** hydrogenolysis (190° C, 2.0 atm H_2 0.12 mol% Zr). (**E**) GC/MS chromatograms of DCM extracts from **i-PP** experiments. (**F**) Temporal product distributions for **AlS/ZrNp$_2$**-catalyzed **PECO** hydrogenolysis (190° C, 2.0 atm H_2, 0.07 mol% Zr). (**G**) GC/MS chromatograms of DCM extracts from **PECO** experiments.

Reaction Mechanism (Details in Supplementary Materials).

Early transition metal d^0 reaction pathways differ distinctly from most later metal systems, and frequently involve combinations of four-center σ-bond metathesis and/or C=C/X=X

insertion/extrusion. For the challenging cleavage of polyolefin C-C bonds, as mediated by the present very unusual surface catalyst, two turnover-limiting pathways were examined: 1) σ-bond metathesis (*23, 24*) and 2) *ß*-alkyl transfer (*37, 38*). From the present empirical rate law, $v = k[Zr]^1[H_2]^0[\mathbf{C16}]^0$, with [**C16**] in large excess, we infer that the turnover-limiting step or any preceding steps in rapid equilibrium, do not involve direct H_2 attack at the catalytic center. From the adsorbate structures, kinetic data, control experiments, and literature precedent, DFT reaction coordinates were computed for scenarios 1) and 2) using *n*-dodecane as a model, in **Figures 4A** and **4B,** respectively (*19,20*). As for catalyst choice, note that a multitude of **AlS/ZrH(R)** species (R= alkyl or H) of similar energies are doubtless equilibrating *via* C-H σ-bond metathesis processes (**Fig. 4C**). **AlS/ZrH$_2$** was selected for simplicity however similar pathways are conceivable for other **AlS/ZrH(R)** species. For C-C scission *via* σ-bond metathesis (**Fig. 4A**), this pathway surprisingly has a prohibitive 76 kcal/mol barrier. Indeed, an experiment with ethane over a relatively high **AlS/ZrH(Np)** loading (0.9% mol Zr), reveals negligible hydrogenolysis at 150°C/1 h (**Eq. 1**).

$$H_3C{-}CH_3 + H_2 \xrightarrow[150°C,\ 1h]{\text{AlS/ZrNpH, 0.9 mol\% Zr}} 2\,CH_4 \qquad (1)$$

In contrast, a Zr-*sec*-dodecyl complex is readily accessed *via* C-H σ-bond activation/metathesis of *n*-dodecane (H_2 elimination step in **Fig. 4B**) and is the lowest energy intermediate found on the reaction coordinate (catalyst resting state), in agreement with the experimental zero-order rate law dependence on alkane concentration. Primary or secondary C-H activation is comparably exergonic with $\Delta G \approx -5$ kcal/mol. Secondary activation on a polyolefin chain seems statistically more probable, with the intermediate then undergoing intramolecular *ß*-alkyl transfer, yielding a Zr-alkyl and olefin (**Fig. 4B**; $\Delta G = +14.5$ kcal/mol). Here $\Delta G^{\ddagger} = 26.1$ kcal/mol barrier and is rate-limiting for chain shortening. In principle this process is reversible, and the olefin can reinsert, explaining the ~1% methyl branches in the products. The next step in this sequence is Zr-C bond hydrogenolysis with a 11.0 kcal/mol barrier to yield a Zr dihydride. This step is slightly endergonic ($\Delta G = 0.6$ kcal/mol) and yields shorter alkanes. Note that the barrier for Zr-C bond hydrogenolysis is slightly lower than the *ß*-alkyl transfer step and therefore is not expected to be rate-limiting, in agreement with the experimental zero-order rate law dependence on H_2 concentration. Experimentally, alkenes are not detected at any stage in the reaction, and the DFT modeling shows that any alkene produced from *ß*-alkyl transfer rapidly insert into a Zr-H bond in a barrierless, strongly exergonic step ($\Delta G = -24.2$ kcal/mol), and the product is then hydrogenolyzed. Therefore, overall alkane hydrogenolysis is computed to be exergonic by $\Delta G = -14.3$ kcal/mol. While this reverse of single-site polymerization producing smaller alkenes from a longer polyalkane chain is endergonic, the coupled olefin hydrogenation renders the overall alkane, and by inference, polyethylene deconstruction, decidedly exergonic. Note that identifying **AlS/ZrH(Np)**-catalyzed *ß*-alkyl transfer as the key turnover-limiting step consistent with experiment has implications for other polymers and other electrophilic transition metal catalysts.

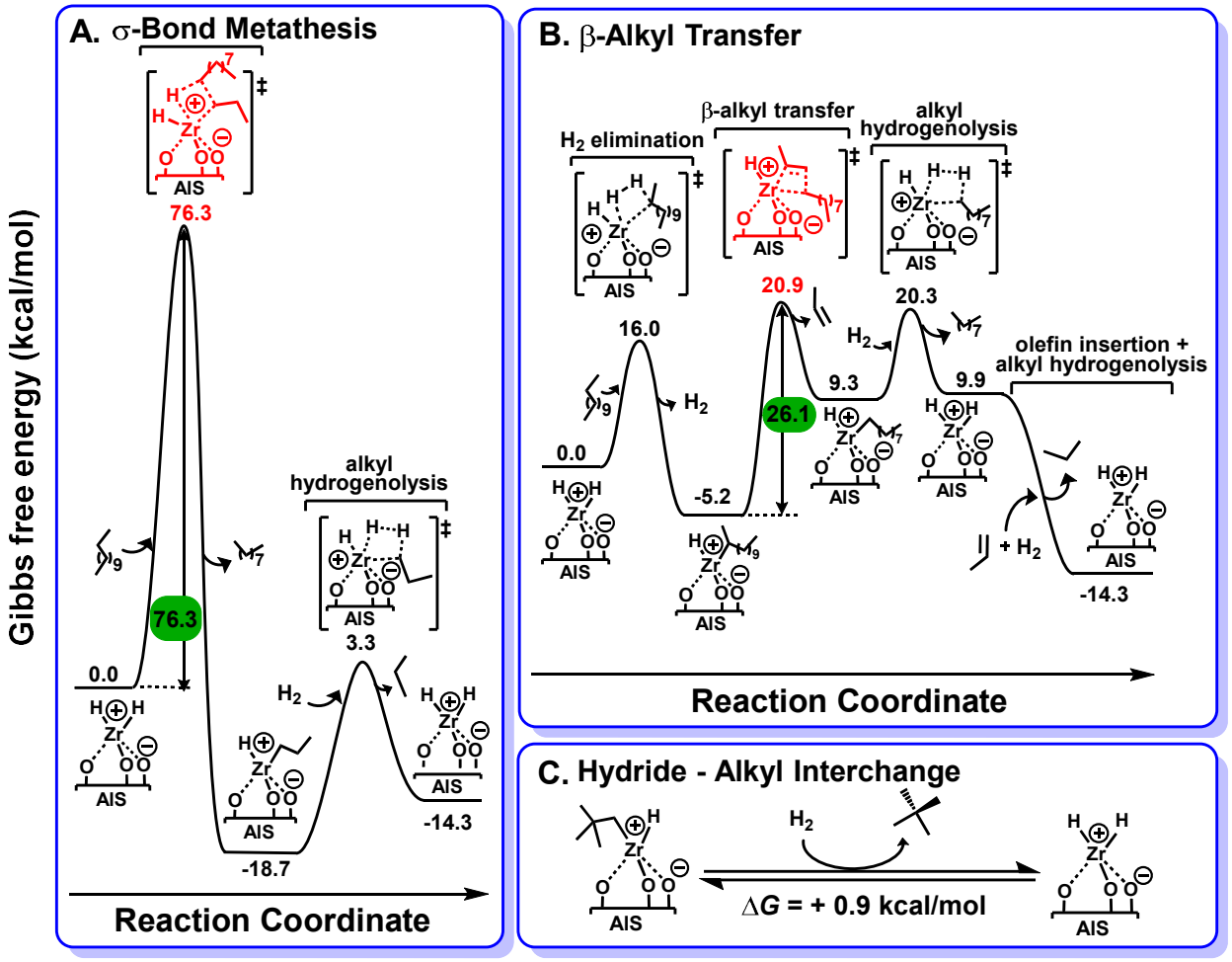

Fig. 4. Computed reaction coordinates for AlS/ZrH$_2$-catalyzed *n*-dodecane hydrogenolysis *via* plausible turnover-limiting pathways, (**A**) C-C scission *via* four-center σ-bond metathesis, (**B**) C-C scission *via* intramolecular *β*-alkyl transfer, (**C**) Representative computed energetics for Zr alkyl/hydride ligand interchange.

Conclusions

A single-site cationic Zr-alkyl catalyst was synthesized on highly Brønsted acidic sulfated alumina and characterized by solid-state ^{1}H MAS and ^{13}C CPMAS-NMR, DRIFTS, ICP/AES, XANES, EXAFS, DFT, and evaluated for hexadecane (**C16**) and polyolefin hydrogenolysis. This catalyst mediates rapid (690 mol **C16** · mol Zr^{-1} · h^{-1}) hexadecane hydrogenolysis under relatively mild conditions (150 °C / 2.5 atm H$_2$). Under similar solventless conditions, polyethylene, polyethylene-*co*-1-octene, isotactic polypropylene, and commercial PE are rapidly hydrogenolyzed to low molecular mass hydrocarbons under mild conditions (150 °C-190 °C/ 2 atm H$_2$) at low catalyst loadings (0.06 mol% Zr). Experimental results combined with DFT computation reveal that the turnover-limiting step in alkane/polyolefin C-C scission/chain shortening is intramolecular *β*-alkyl transfer, in contrast to the σ-bond metathesis process common in much early transition metal catalytic chemistry. The catalytic species, a supported electrophilic Zr-hydride, is readily formed during the hydrogenolysis process. These results convey implications for deconstructing other polymers and the catalysts to achieve this.

References and Notes

1. Ellen MacArthur Foundation (2017). *The new plastics economy: rethinking the future of plastics & catalysing action.*
2. R. Geyer, J. R. Jambeck, K. L. Law, Production, use, and fate of all plastics ever made. *Sci. Adv.* **3**, e1700782 (2017).
3. A. D. Vethaak, J. Legler, Microplastics and human health. *Science* **371**, 672 (2021).
4. J. R. Jambeck, R. Geyer, C. Wilcox, T. R. Siegler, M. Perryman, A. Andrady, R. Narayan, K. L. Law, Plastic waste inputs from land into the ocean. *Science* **347**, 768 (2015).
5. J. P. Lange, Towards circular carbo-chemicals – the metamorphosis of petrochemicals. *Energy Environ. Sci.* **14**, 4358-4376 (2021).
6. J. M. Garcia, M. L. Robertson, The future of plastics recycling. *Science* **358**, 870-872 (2017).
7. M. Hong, E. Y. X. Chen, Chemically recyclable polymers: a circular economy approach to sustainability. *Green Chem.* **19**, 3692-3706 (2017).
8. K. Ragaert, L. Delva, K. Van Geem, Mechanical and chemical recycling of solid plastic waste. *Waste Manag.* **69**, 24-58 (2017).
9. I. Vollmer, M. J. F. Jenks, M. C. P. Roelands, R. J. White, T. van Harmelen, P. de Wild, G. P. van der Laan, F. Meirer, J. T. F. Keurentjes, B. M. Weckhuysen, Beyond Mechanical Recycling: Giving New Life to Plastic Waste. *Angew. Chem. Int. Ed.* **59**, 15402-15423 (2020).
10. X. Jia, C. Qin, T. Friedberger, Z. Guan, Z. Huang, Efficient and selective degradation of polyethylenes into liquid fuels and waxes under mild conditions. *Sci. Adv.* **2**, e1501591 (2016).
11. G. Celik, R. M. Kennedy, R. A. Hackler, M. Ferrandon, A. Tennakoon, S. Patnaik, A. M. LaPointe, S. C. Ammal, A. Heyden, F. A. Perras, M. Pruski, S. L. Scott, K. R. Poeppelmeier, A. D. Sadow, M. Delferro, Upcycling Single-Use Polyethylene into High-Quality Liquid Products. *ACS Cent. Sci.* **5**, 1795-1803 (2019).
12. F. Zhang, M. Zeng, R. D. Yappert, J. Sun, Y. H. Lee, A. M. LaPointe, B. Peters, M. M. Abu-Omar, S. L. Scott, Polyethylene upcycling to long-chain alkylaromatics by tandem hydrogenolysis/aromatization. *Science* **370**, 437-441 (2020).
13. J. E. Rorrer, G. T. Beckham, Y. Román-Leshkov, Conversion of Polyolefin Waste to Liquid Alkanes with Ru-Based Catalysts under Mild Conditions. *JACS Au* **1**, 8-12 (2020).
14. P. A. Kots, S. Liu, B. C. Vance, C. Wang, J. D. Sheehan, D. G. Vlachos, Polypropylene Plastic Waste Conversion to Lubricants over Ru/TiO_2 Catalysts. *ACS Catal.* **11**, 8104-8115 (2021).
15. C. Jia, S. Xie, W. Zhang, N. N. Intan, J. Sampath, J. Pfaendtner, H. Lin, Deconstruction of high-density polyethylene into liquid hydrocarbon fuels and lubricants by hydrogenolysis over Ru catalyst. *Chem Catalysis* **1**, 437-455 (2021).
16. A. Tennakoon, X. Wu, A. L. Paterson, S. Patnaik, Y. Pei, A. M. LaPointe, S. C. Ammal, R. A. Hackler, A. Heyden, I. I. Slowing, G. W. Coates, M. Delferro, B. Peters, W. Huang, A. D. Sadow, F. A. Perras, Catalytic upcycling of high-density polyethylene via a processive mechanism. *Nat. Catal* **3**, 893-901 (2020).

17. L. D. Ellis, S. V. Orski, G. A. Kenlaw, A. G. Norman, K. L. Beers, Y. Román-Leshkov, G. T. Beckham, Tandem Heterogeneous Catalysis for Polyethylene Depolymerization via an Olefin-Intermediate Process. *ACS Sustain. Chem. Eng.* **9**, 623-628 (2021).
18. V. R. Dufaud, J. M. Basset, Catalytic hydrogenolysis at low temperature and pressure of polyethylene and polypropylene to diesels or lower alkanes by a zirconium hydride supported on silica-alumina: A step toward polyolefin degradation by the microscopic reverse of Ziegler-Natta polymerization. Angew. Chem. Int. Ed. **37**, 806-810 (1998). From the data reported, we estimate the activity to be ca. 2% of that in Table 2 entry 6.
19. L. A. Williams, N. Guo, A. Motta, M. Delferro, I. L. Fragalà, J. T. Miller, T. J. Marks, Surface structural-chemical characterization of a single-site d0 heterogeneous arene hydrogenation catalyst having 100% active sites. *PNAS* **110**, 413 (2013).
20. W. Gu, M. M. Stalzer, C. P. Nicholas, A. Bhattacharyya, A. Motta, J. R. Gallagher, G. Zhang, J. T. Miller, T. Kobayashi, M. Pruski, M. Delferro, T. J. Marks, Benzene Selectivity in Competitive Arene Hydrogenation: Effects of Single-Site Catalyst···Acidic Oxide Surface Binding Geometry. *J. Am. Chem. Soc.* **137**, 6770-6780 (2015).
21. M. M. Stalzer, M. Delferro, T. J. Marks, Supported Single-Site Organometallic Catalysts for the Synthesis of High-Performance Polyolefins. *Catal. Lett.* **145**, 3-14 (2015).
22. K. Arata, M. Hino, Solid catalyst treated with anion: XVIII. Benzoylation of toluene with benzoyl chloride and benzoic anhydride catalysed by solid superacid of sulfate-supported alumina. *Appl. Catal.* **59**, 197-204 (1990).
23. J. A. Labinger, J. E. Bercaw, Understanding and exploiting C–H bond activation. *Nature* **417**, 507-514 (2002).
24. R. Waterman, σ-Bond Metathesis: A 30-Year Retrospective. *Organometallics* **32**, 7249-7263 (2013).
25. F. Rataboul, A. Baudouin, C. Thieuleux, L. Veyre, C. Coperet, J. Thivolle-Cazat, J. M. Basset, A. Lesage, L. Emsley, Molecular understanding of the formation of surface zirconium hydrides upon thermal treatment under hydrogen of [([triple bond]SiO)Zr(CH2tBu)$_3$] by using advanced solid-state NMR techniques. *J. Am. Chem. Soc.* **126**, 12541-12550 (2004).
26. N. Eedugurala, Z. Wang, U. Chaudhary, N. Nelson, K. Kandel, T. Kobayashi, I. I. Slowing, M. Pruski, A. D. Sadow, Mesoporous Silica-Supported Amidozirconium-Catalyzed Carbonyl Hydroboration. *ACS Catal.* **5**, 7399-7414 (2015).
27. X. Yang, C. L. Stern, T. J. Marks, Cationic Metallocene Polymerization Catalysts. Synthesis and Properities of the First Base-Free Zirconocene Hydride. *Angew. Chem. Int. Ed. Engl.* **31**, 1375-1377 (1992).
28. K. C. Szeto, N. Merle, J. Trébosc, M. Taoufik, R. M. Gauvin, F. Pourpoint, L. Delevoye, Caveat on the Actual Robustness of Heteronuclear NMR Methods for Probing the Surface of γ-Alumina and Related Catalysts. *J. Phys. Chem. C* . **123**, 12919-12927 (2019).
29. B. Werghi, A. Bendjeriou-Sedjerari, A. Jedidi, E. Abou-Hamad, L. Cavallo, J.-M. Basset, Single-Site Tetracoordinated Aluminum Hydride Supported on Mesoporous Silica. From Dream to Reality! *Organometallics* **35**, 3288-3294 (2016).
30. S. L. Latesky, A. K. McMullen, G. P. Niccolai, I. P. Rothwell, J. C. Huffman, The chemistry of sterically crowded aryl oxide ligands. 3. Crystal and molecular structure and spectroscopic properties of mixed benzyl-aryl oxide compounds of zirconium. *Organometallics* **4**, 902-908 (1985).
31. G. B. Nikiforov, H. W. Roesky, T. Schulz, D. Stalke, M. Witt, On the quest for new mixed-metal mu-oxo-bridged complexes: synthesis of compounds containing transition

metal-oxygen-main group metal motifs M-O-M1 (M = Ti, Zr; M1 = Al, Ga) without cyclopentadienyl ligands. *Inorg. Chem.* **47**, 6435-6443 (2008).

32. J. Corker, F. Lefebvre, C. Lecuyer, V. Dufaud, F. Quignard, A. Choplin, J. Evans, J. M. Basset, Catalytic cleavage of the C-H and C-C bonds of alkanes by surface organometallic chemistry: An EXAFS and IR characterization of a Zr-H catalyst. *Science* **271**, 966-969 (1996).
33. J. Zhang, A. H. Mason, A. Motta, L. G. Cesar, Y. Kratish, T. L. Lohr, J. T. Miller, Y. Gao, T. J. Marks, Surface vs Homogeneous Organo-Hafnium Catalyst Ion-Pairing and Ligand Effects on Ethylene Homo- and Copolymerizations. *ACS Catal.* **11**, 3239-3250 (2021).
34. J. Zhang, A. H. Mason, Y. Wang, A. Motta, T. Kobayashi, M. Pruski, Y. Gao, T. J. Marks, Beyond the Active Site. Cp*ZrMe3/Sulfated Alumina-Catalyzed Olefin Polymerization Tacticity via Catalyst···Surface Ion-Pairing. *ChemCatChem* **13**, 2564-2569 (2021).
35. T. A. Manz, N. G. Limas, Introducing DDEC6 atomic population analysis: part 1. Charge partitioning theory and methodology. *RSC Adv.* **6**, 47771-47801 (2016).
36. H. P. Kiran Pulidindi, "Linear Low-Density Polyethylene (LLDPE) Market Size By Application (Films, Injection Molding, Rotomolding), Industry Analysis Report, Regional Outlook, Growth Potential, Price Trends, Competitive Market Share & Forecast, 2016 – 2024," (2017).
37. M. E. O'Reilly, S. Dutta, A. S. Veige, β-Alkyl Elimination: Fundamental Principles and Some Applications. *Chem. Rev.* **116**, 8105-8145 (2016).
38. X. Yang, L. Jia, T. J. Marks, Carbon-carbon activation at electrophilic d0/fn centers. Facile, regioselective .beta.-alkyl shift-based ring-opening polymerization reactions of methylenecyclobutane. *J. Am. Chem. Soc.* **115**, 3392-3393 (1993).
39. T. D. Kühne, M. Iannuzzi, M. Del Ben, V. V. Rybkin, P. Seewald, F. Stein, T. Laino, R. Z. Khaliullin, O. Schütt, F. Schiffmann, D. Golze, J. Wilhelm, S. Chulkov, M. H. Bani-Hashemian, V. Weber, U. Borštnik, M. Taillefumier, A. S. Jakobovits, A. Lazzaro, H. Pabst, T. Müller, R. Schade, M. Guidon, S. Andermatt, N. Holmberg, G. K. Schenter, A. Hehn, A. Bussy, F. Belleflamme, G. Tabacchi, A. Glöß, M. Lass, I. Bethune, C. J. Mundy, C. Plessl, M. Watkins, J. VandeVondele, M. Krack, J. Hutter, CP2K: An electronic structure and molecular dynamics software package -Quickstep: Efficient and accurate electronic structure calculations. *J. Chem. Phys.* **152**, 194103 (2020).
40. J. VandeVondele, J. Hutter, Gaussian basis sets for accurate calculations on molecular systems in gas and condensed phases. *J. Chem. Phys.* **127**, 1–9 (2007).
41. S. Goedecker, M. Teter, J. Hutter, Separable Dual-Space Gaussian Pseudopotentials. *Phys. Rev. B*. **54**, 1703–1710 (1996).
42. J. P. Perdew, K. Burke, M. Ernzerhof, Generalized Gradient Approximation Made Simple. *Phys. Rev. Lett.* **77**, 3865–3868 (1996).
43. S. Grimme, J. Antony, S. Ehrlich, H. Krieg, A consistent and accurate ab initio parametrization of density functional dispersion correction (DFT-D) for the 94 elements H-Pu. *J. Chem. Phys.* **132**, 1–19 (2010).
44. Chemcraft - graphical software for visualization of quantum chemistry computations. https://www.chemcraftprog.com.

45. M. J. Frisch, G. W. Trucks, H. B. Schlegel, G. E. Scuseria, M. A. Robb, J. R. Cheeseman, G. Scalmani, V. Barone, G. A. Petersson, H. Nakatsuji, X. Li, M. Caricato, A. V Marenich, J. Bloino, B. G. Janesko, R. Gomperts, B. Mennucci, H. P. Hratchian, J. V Ortiz, A. F. Izmaylov, J. L. Sonnenberg, D. Williams-Young, F. Ding, F. Lipparini, F. Egidi, J. Goings, B. Peng, A. Petrone, T. Henderson, D. Ranasinghe, V. G. Zakrzewski, J. Gao, N. Rega, G. Zheng, W. Liang, M. Hada, M. Ehara, K. Toyota, R. Fukuda, J. Hasegawa, M. Ishida, T. Nakajima, Y. Honda, O. Kitao, H. Nakai, T. Vreven, K. Throssell, J. A. Montgomery Jr., J. E. Peralta, F. Ogliaro, M. J. Bearpark, J. J. Heyd, E. N. Brothers, K. N. Kudin, V. N. Staroverov, T. A. Keith, R. Kobayashi, J. Normand, K. Raghavachari, A. P. Rendell, J. C. Burant, S. S. Iyengar, J. Tomasi, M. Cossi, J. M. Millam, M. Klene, C. Adamo, R. Cammi, J. W. Ochterski, R. L. Martin, K. Morokuma, O. Farkas, J. B. Foresman, D. J. Fox, Gaussian 16 Revision B.01 (2016).

Acknowledgments:

Financial support was provided by the U.S. Department of Energy, Office of Science, Office of Basic Energy Sciences under Award Number DOE DE-FG02-03ER15457 to the Institute for Catalysis in Energy Processes (ICEP) at Northwestern University (NU). This work made use of IMSERC facilities at NU, which have received support from Soft and Hybrid Nanotechnology Experimental (SHyNE) Resource (NSF ECCS-2025633), Int. Institute of Nanotechnology (IIN), and NU. This work made use of the NU QBIC supported by NASA Ames Research Center Grant NNA04CC36G. This work made use of the REACT Facility of NU's Center for Catalysis and Surface Science supported by a grant from the DOE (DE-SC0001329). This work used the DuPont-Northwestern-Dow Collaborative Access Team (DND-CAT) 5BM-D beamline at the Advanced Photon Source (APS). DND-CAT is supported by NU, E. I. DuPont de Nemours & Co., and The Dow Chemical Company. APS is supported by DOE at Argonne National Laboratory under Contract No. DE-AC02-06CH11357. This research was supported in part by the computational resources and staff contributions provided by the Quest High Performance Computing Facility at NU, which is jointly supported by the Office of the Provost, the Office for Research, and NU Information Technology. We thank Dr. J. Li for insightful discussions of reaction kinetics and Dr. Robert Pankow for his diligent effort in repairing, maintaining, and training students on the GPC

Author contributions:

AHM, YK, TJM conceived the ideas and designed experiments.

AHM performed most experiments with aid from YK.

AM performed the DFT analysis.

QM performed the XANES/EXAFS experiments.

AD analyzed the XANES/EXAFS data with guidance from MJB.

AHM, YK, TJM wrote the manuscript.

Competing interests:

Authors declare that they have no competing interests.

Data and materials availability:

All data are available in the main text or Supplementary Materials.

Supplementary Materials

Materials and Methods

Supplementary Text

Figs. S1 - S16

Table S1-S2

References 39 - 45

Video S1